Supplement of Biogeosciences, 20, 4197–4212, 2023
https://doi.org/10.5194/bg-20-4197-2023-supplement
© Author(s) 2023. CC BY 4.0 License.

Biogeosciences Open Access EGU

Supplement of

The fingerprint of climate variability on the surface ocean cycling of iron and its isotopes

Daniela König and Alessandro Tagliabue

Correspondence to: Daniela König (dkoenig@hawaii.edu)

The copyright of individual parts of the supplement might differ from the article licence.

Text S1.

Exemplary Fe isotope model equations

Equations 1 to 5 illustrate how Fe isotopes were included in the PISCES model using heavy ($^{56}Fe_{diss}$) and light ($^{54}Fe_{diss}$) dFe as an example. Note that other Fe tracers (i.e., small/large Fe particles; nanophytoplankton and diatom Fe) are modelled similarly as dFe, although without any external supply terms.

	External Fe supply	Internal transformation without fractionation	Internal transformation with fractionation	
$\frac{\partial^{56}Fe_{diss}}{\partial t} =$	$J_{dust,Fe} * \frac{R_{dust,Fe}}{R_{dust,Fe}+1}$	$+ J_{remin,Fe} * \frac{R_{Fe,part}}{R_{Fe,part}+1}$	$- J_{up,Fe} * \frac{R_{Fe,diss} * \alpha_{up}}{R_{Fe,diss} * \alpha_{up}+1}$	(1)
$\frac{\partial^{54}Fe_{diss}}{\partial t} =$	$J_{dust,Fe} * \frac{1}{R_{dust,Fe}+1}$	$+ J_{remin,Fe} * \frac{1}{R_{Fe,part}+1}$	$- J_{up,Fe} * \frac{1}{R_{Fe,diss} * \alpha_{up}+1}$	(2)

$$R_{dust,Fe} = \frac{^{56}Fe_{IRMM-014}}{^{54}Fe_{IRMM-014}} * \left(\frac{\delta^{56}Fe_{dust}}{1000} + 1\right) \quad (3)$$

$$R_{Fe,part} = \frac{^{56}Fe_{part}}{^{54}Fe_{part}} \quad (4)$$

$$R_{Fe,diss} = \frac{^{56}Fe_{diss}}{^{54}Fe_{diss}} \quad (5)$$

$J_{dust,Fe}$	Dissolved Fe supply rate from dust
$R_{dust,Fe}$	Isotope ratio of supplied dust Fe
$\delta^{56}Fe_{dust}$	Endmember signature of dust Fe supply
$J_{remin,Fe}$	Dissolved Fe supply by remineralisation of Fe particles
$R_{Fe,part}$	Isotope ratio of Fe particles, see eq. 5
$^{56}Fe_{part}$	Heavy particulate Fe concentration
$^{54}Fe_{part}$	Light particulate Fe concentration
$J_{up,Fe}$	dissolved Fe uptake by phytoplankton
$R_{Fe,diss}$	Isotope ratio dissolved Fe, see eq. 4
α_{up}	fractionation factor for phytoplankton Fe uptake
$^{56}Fe_{diss}$	Heavy particulate Fe concentration
$^{54}Fe_{diss}$	Light particulate Fe concentration

Input of Fe by external sources (illustrated here for dust dFe supply) is included by multiplying the total Fe flux (e.g., $J_{dust,Fe}$) with the respective fraction of ^{56}Fe and ^{54}Fe of the source, which is calculated from its $\delta^{56}Fe$ endmember (e.g., $\delta^{56}Fe_{dust}$; eq. 3).

Internal transformation processes that do not fractionate isotopes (illustrated for dFe supply by remineralisation of Fe particles) are included by multiplying the amount of transformed Fe (e.g., $J_{remin,Fe}$) with the respective fraction of ^{56}Fe and ^{54}Fe of the transformed tracer (e.g., Fe particles), which is calculated from their ratio (e.g., $R_{Fe,part}$; eq. 4). Internal transformation processes that include isotopic fractionation (illustrated for dFe uptake by phytoplankton) are calculated similarly, whereby the isotope ratio of the transformed Fe tracer (e.g., $R_{Fe,diss}$; eq. 5) is also multiplied with a fractionation factor (e.g., α_{up}) when calculating which fractions of heavy/light Fe are being transferred.

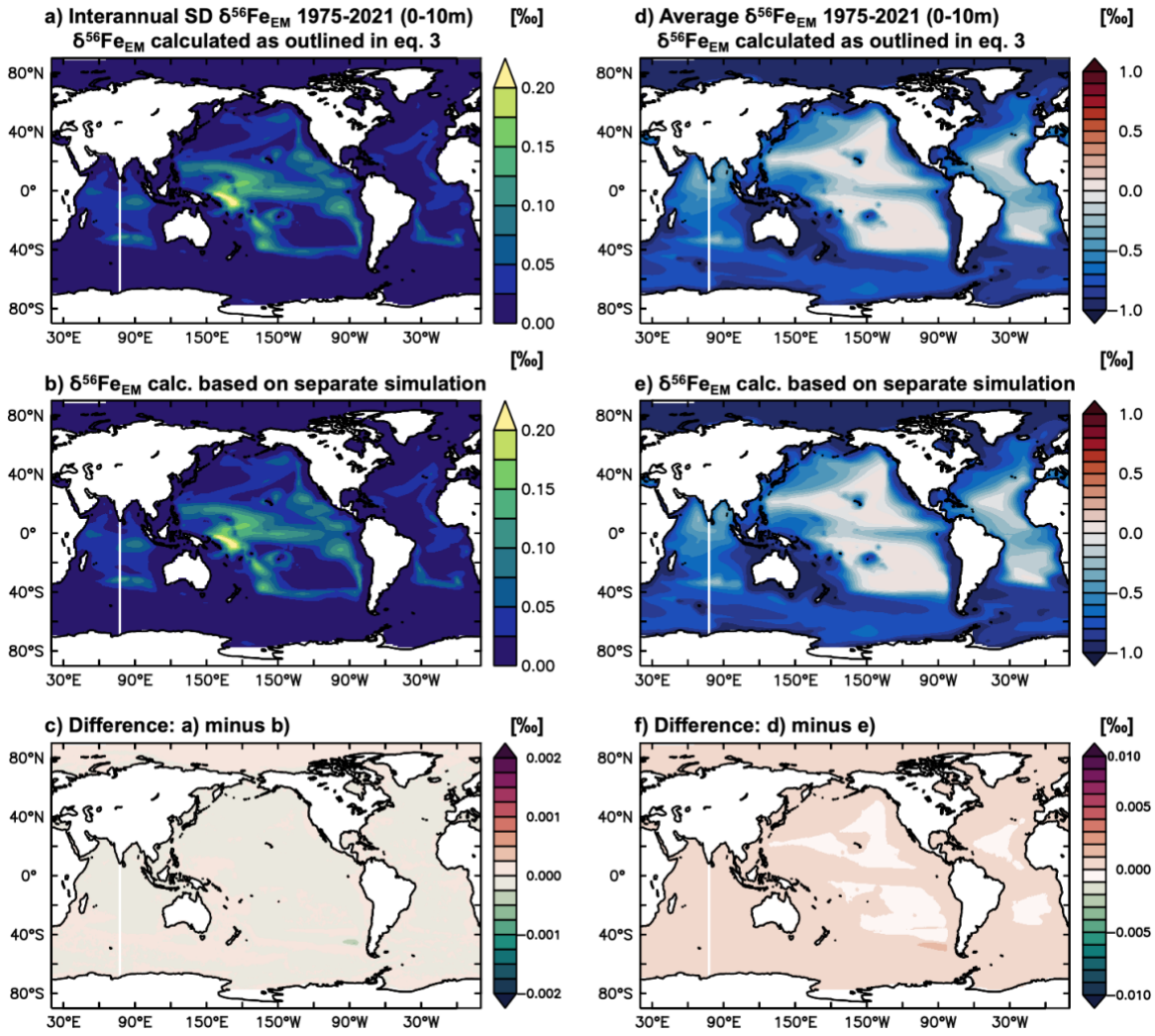

Figure S1. Confirmation of indirect approach to calculate $\delta^{56}Fe_{EM}$, illustrated with surface ocean outputs from hindcast experiments. (a) interannual SD and (b) average value of $\delta^{56}Fe_{EM}$ as calculated from $\delta^{56}Fe_{CF}$ and $\delta^{56}Fe_{UF}$ (Eq. 3); (b) interannual SD and (e) average value of $\delta^{56}Fe_{EM}$ as calculated from a separate experiment with all external source endmembers set to 0‰ using a similar approach as for $\delta^{56}Fe_{UF}$ and $\delta^{56}Fe_{CF}$ in Eq. 1+2. Panels c) and f) show the (negligible) difference between the two approaches for $\delta^{56}Fe_{EM}$ SD and average $\delta^{56}Fe_{EM}$, respectively.

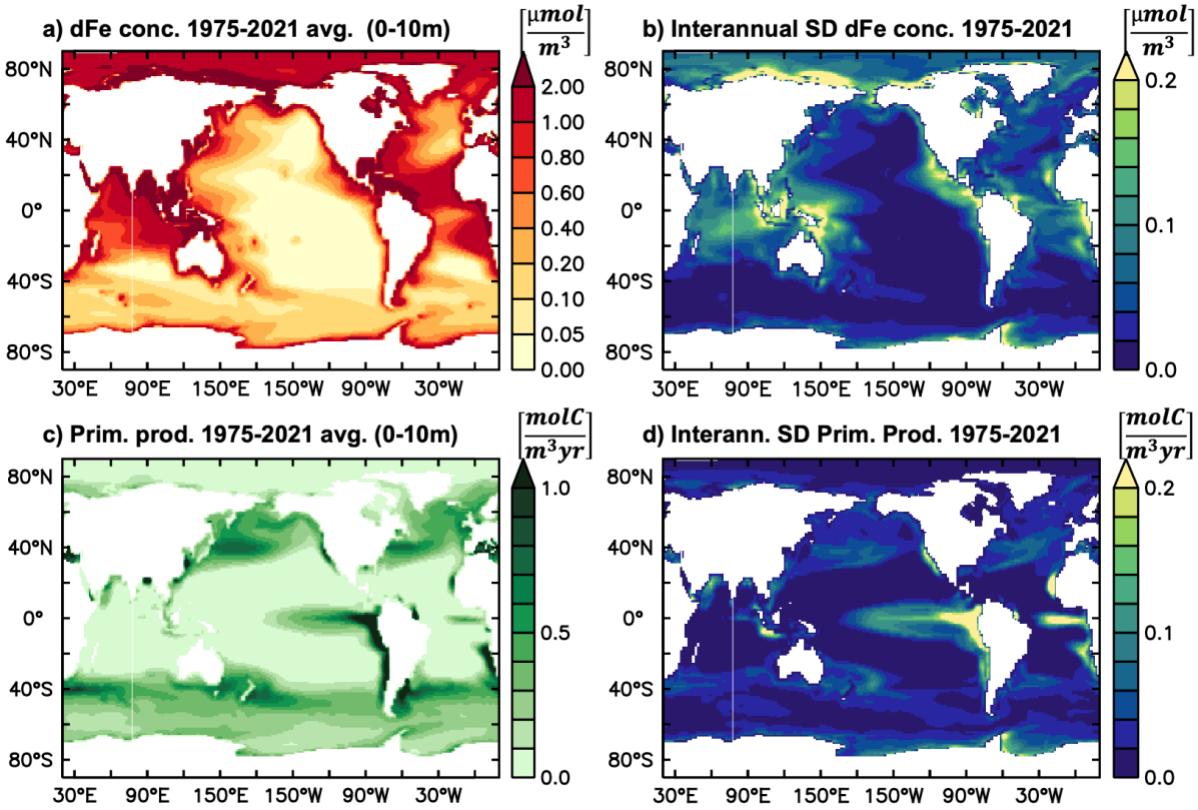

Figure S2. Surface ocean interannual variability of dFe concentration and primary productivity in the present climate (1975-2021). Surface ocean (0-10m) averages and interannual SD of (a,b) dFe concentration and (c,d) primary productivity.

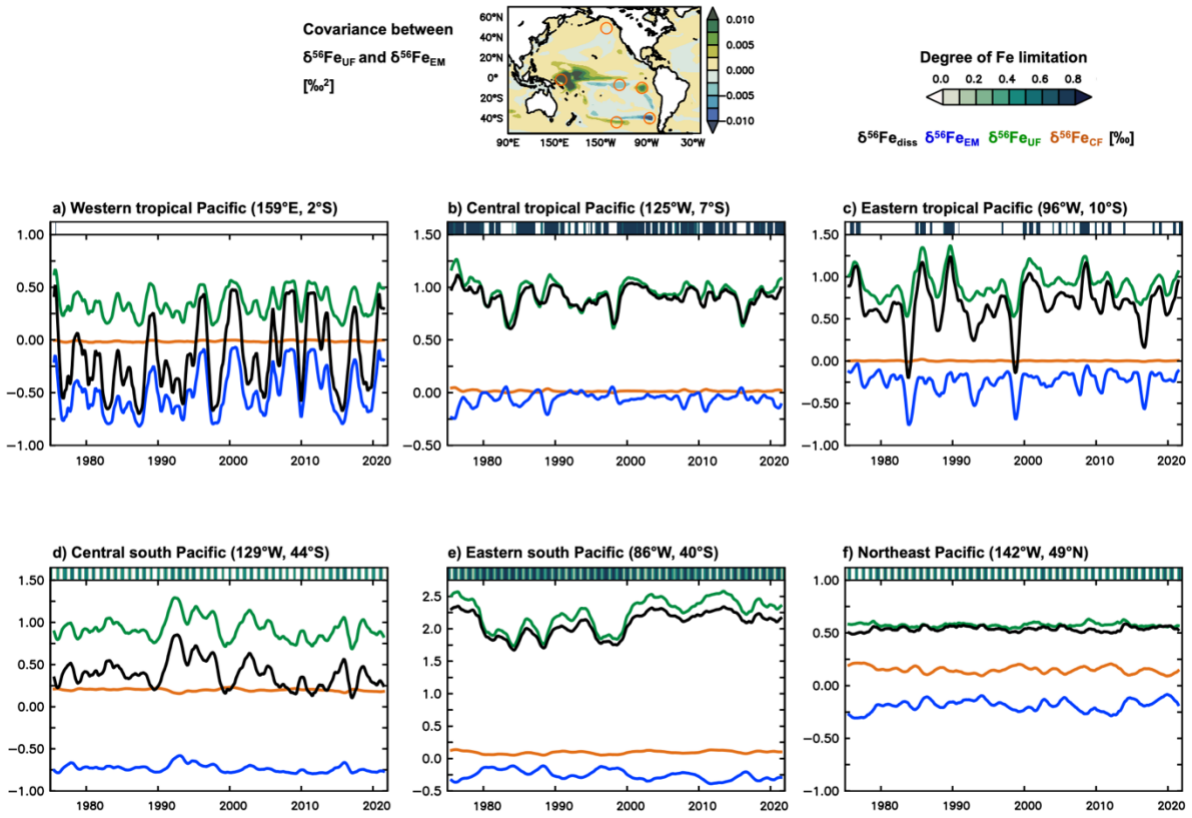

Figure S3. Opposing and reinforcing effects of $\delta^{56}Fe_{diss}$ variability drivers in the present climate. (a-d) Time series of $\delta^{56}Fe_{diss}$, $\delta^{56}Fe_{EM}$, $\delta^{56}Fe_{UF}$ and $\delta^{56}Fe_{CF}$ at four exemplary locations in the tropical and south Pacific, which illustrate how two (or more) drivers (here mainly $\delta^{56}Fe_{EM}$, $\delta^{56}Fe_{UF}$) can have reinforcing (a,c,d; positive covariance) or opposing (b,e,f; negative covariance) effects in time, leading to an increase or decrease in overall $\delta^{56}Fe_{diss}$ variability, respectively. Smaller panels on top show the degree of limitation of phytoplankton. In the tropical Pacific (a-c), $\delta^{56}Fe_{EM}$ and $\delta^{56}Fe_{UF}$ effects reinforce each other in the west (a) and east (c), leading to increased $\delta^{56}Fe_{diss}$ variability, but appear to be out of sync in the central Pacific (c), which somewhat dampens $\delta^{56}Fe_{diss}$ variability. In the south Pacific, $\delta^{56}Fe_{UF}$ and $\delta^{56}Fe_{CF}$ effects reinforce each other in the central, more southern region (d), but oppose each other further north, especially in the eastern part of the basin (e). In the latter, patterns of local Fe limitation also oppose $\delta^{56}Fe_{UF}$, suggesting that these uptake fractionation effects are non-local. Thus, the pattern of $\delta^{56}Fe_{UF}$, $\delta^{56}Fe_{EM}$, and $\delta^{56}Fe_{diss}$ variability in this region may be related to variations in ocean circulation, i.e., variable input of waters from another Fe limited region with high $\delta^{56}Fe_{UF}$, low $\delta^{56}Fe_{EM}$ imprint, most likely in the Southern Ocean. The exemplary station from the Northeast Pacific (f) shows how opposing interannual variability of two drivers ($\delta^{56}Fe_{EM}$ and $\delta^{56}Fe_{CF}$) leads to very little "residual" variability in $\delta^{56}Fe_{diss}$.

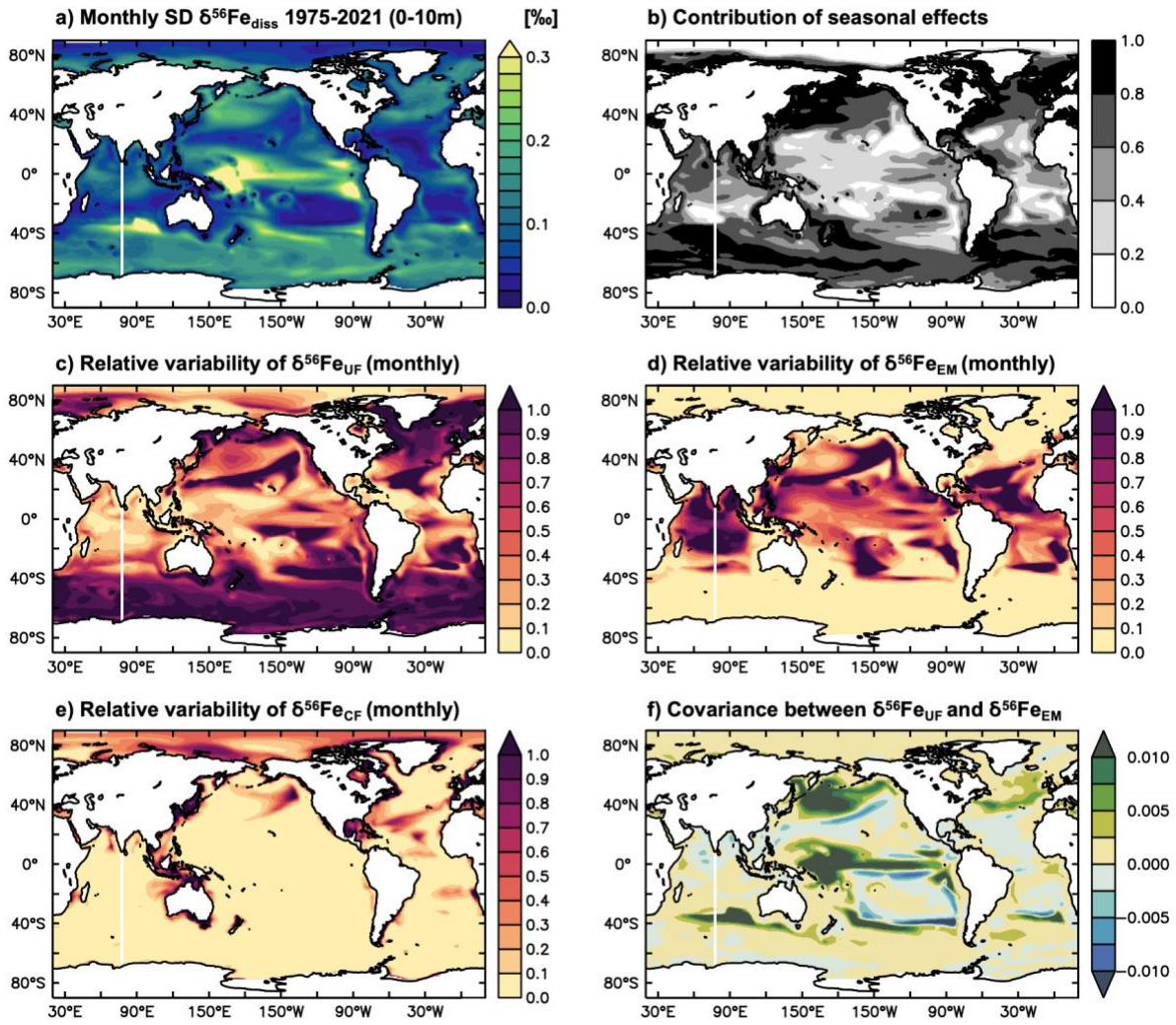

Figure S4: Surface ocean $\delta^{56}Fe_{diss}$ seasonal and interannual variability in the present climate (1975-2021). (a) Surface ocean (0-10m) monthly $\delta^{56}Fe_{diss}$ SD, calculated from monthly hindcast experiment outputs without applying a 12-month running mean. (b) Contribution of seasonal effects to the monthly $\delta^{56}Fe_{diss}$ SD, calculated as follows: $\frac{monthly\ SD\ \delta^{56}Fe_{diss} - interannual\ SD\ \delta^{56}Fe_{diss}}{monthly\ SD\ \delta^{56}Fe_{diss}}$. Ratios of monthly variability of (c) $\delta^{56}Fe_{UF}$, (d) $\delta^{56}Fe_{EM}$, and (e) $\delta^{56}Fe_{CF}$ to the monthly $\delta^{56}Fe_{diss}$ variability, and (f) covariance between $\delta^{56}Fe_{UF}$ and $\delta^{56}Fe_{EM}$ (monthly mean).

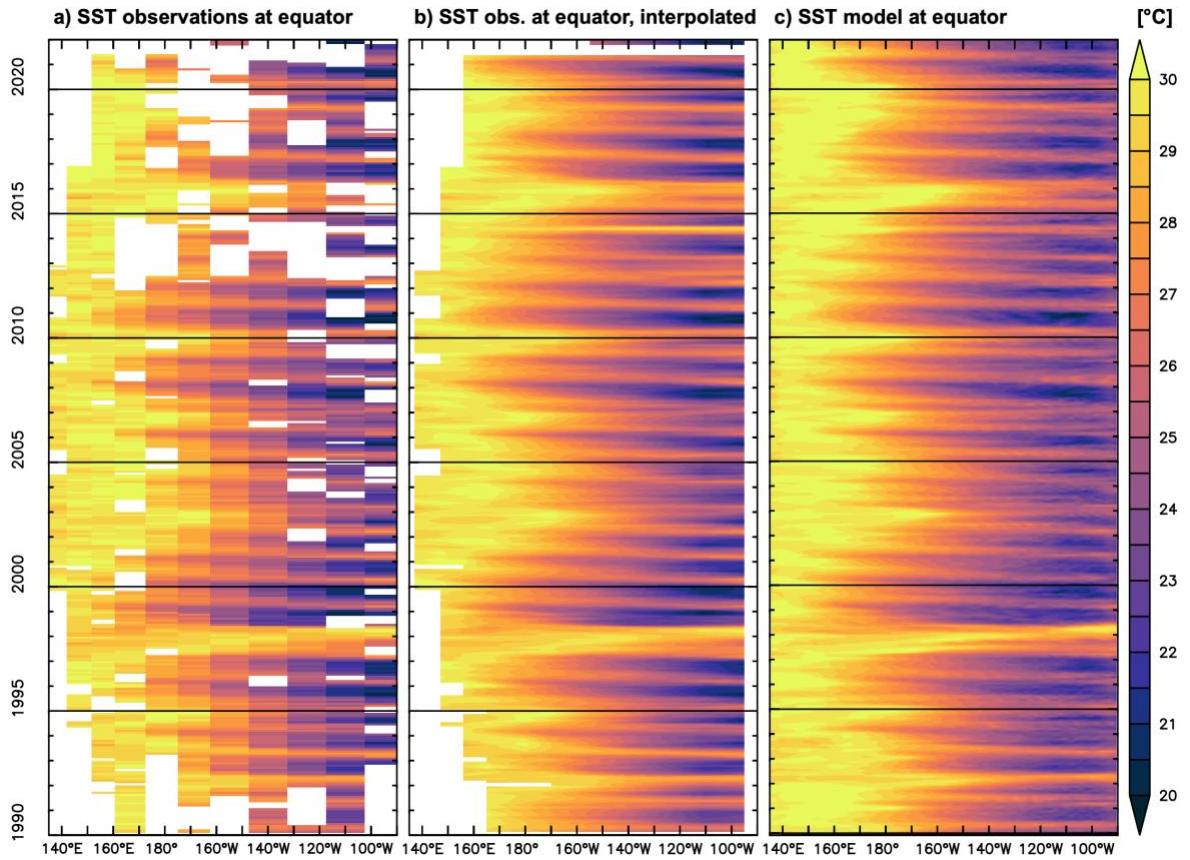

Figure S5: Comparison of hindcast model simulations to observations in the tropical Pacific. (a) Original and (b) interpolated observations of SST at the equator, and (c) the corresponding model output. Monthly-average SST observations were obtained from the TAO/TRITON moored buoy array (TAO Project Office of NOAA/PMEL) for the period of January 1979 to December 2021. A statistical comparison of the hindcast model output to the entire TAO/TRITON SST data (i.e., including data north/south of the equator) shows excellent agreement (R: 0.98, RMSE: 0.46°C).

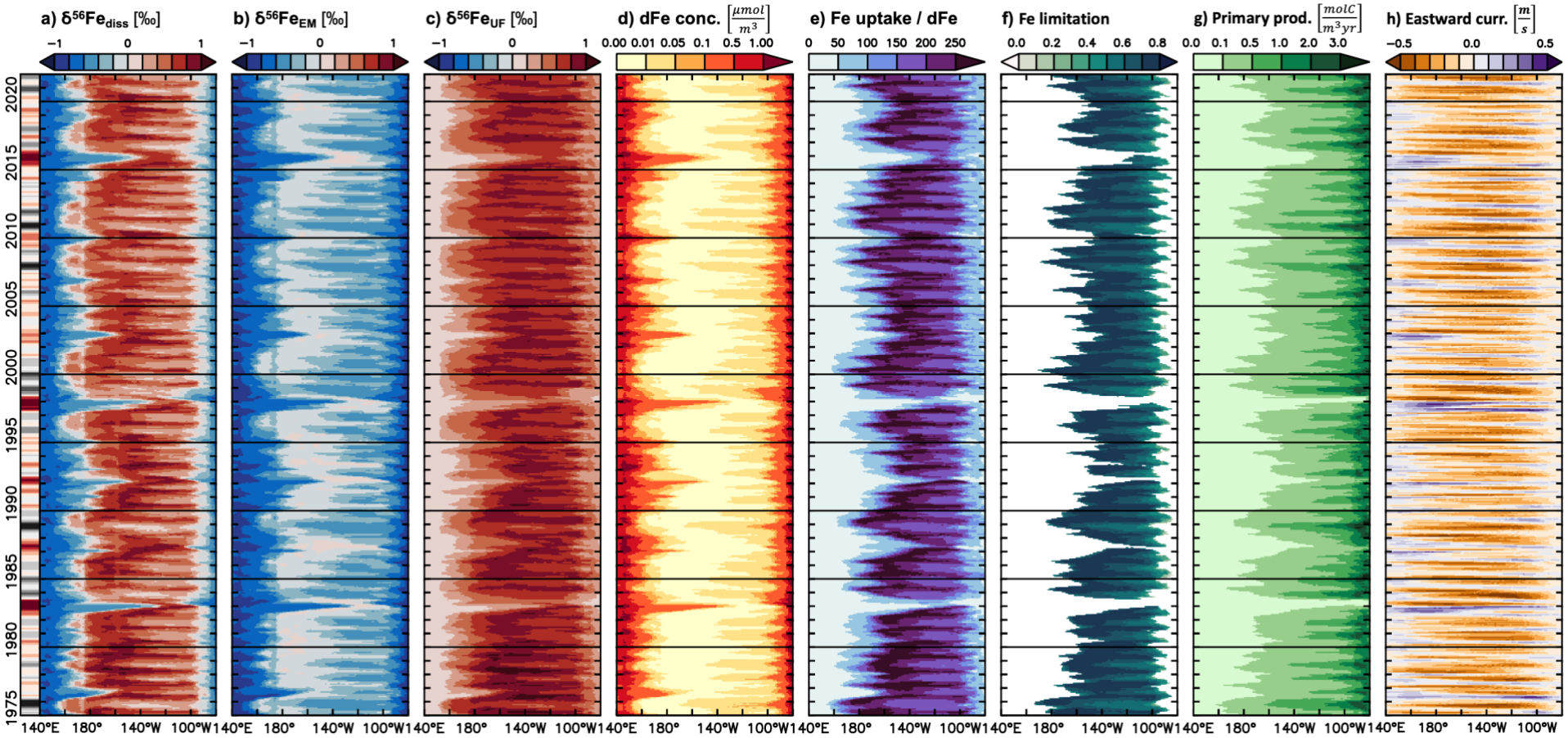

Figure S6: Mechanisms behind surface ocean $\delta^{56}Fe_{diss}$ changes in the equatorial Pacific. Time series (1975-2021) of monthly-mean surface ocean (a) $\delta^{56}Fe_{diss}$, (b) $\delta^{56}Fe_{EM}$, (c) $\delta^{56}Fe_{UF}$, (d) dFe concentration, (e) ratio between Fe uptake and dFe concentration, (f) Fe limitation, (g) primary production, and (d) upper ocean (0-50m average) eastward currents of the hindcast experiments, averaged from 5°N to 5°S. The Ocean Nino Index is included on the left side (red: El Niño, Grey: La Niña).

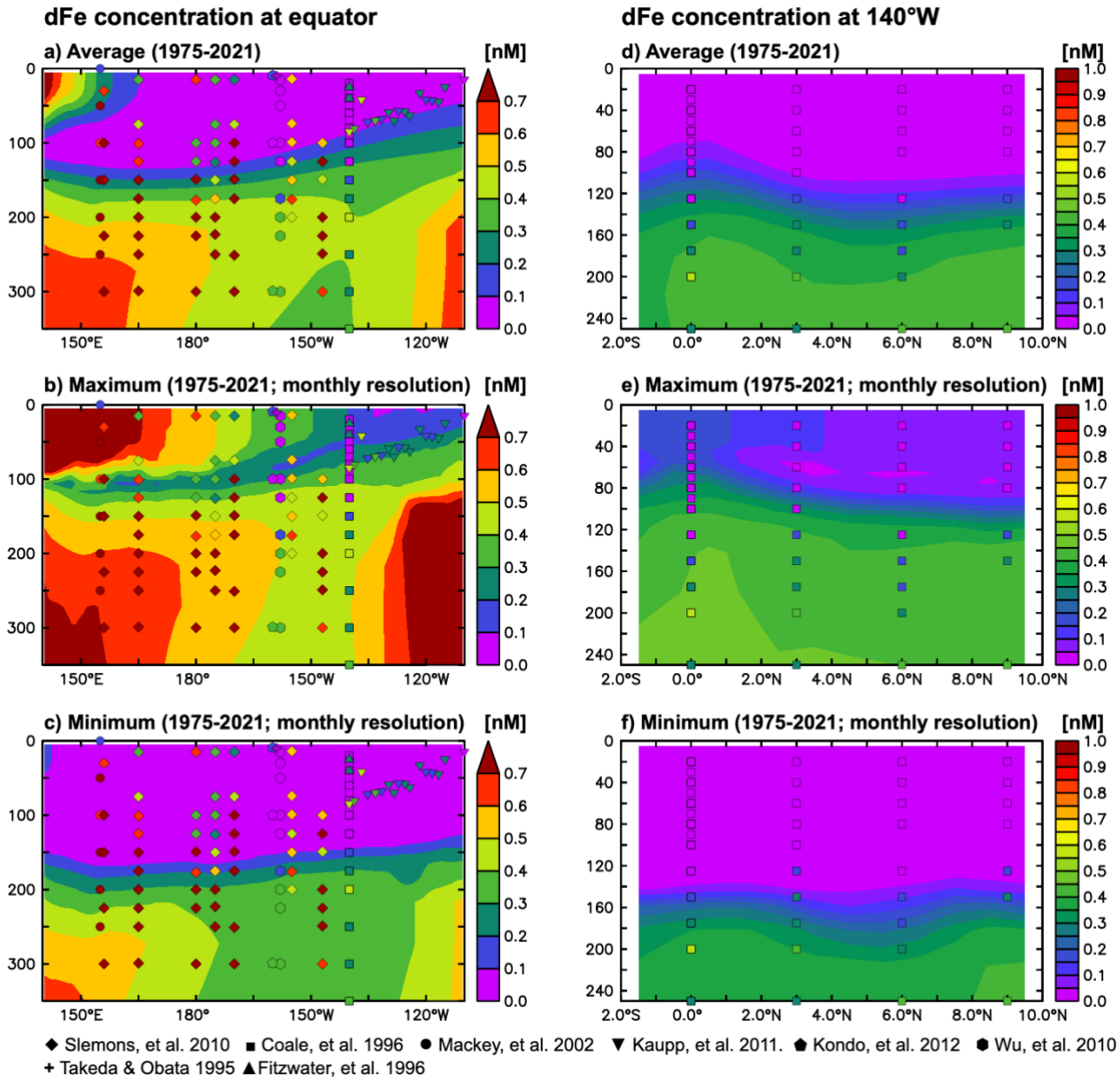

Figure S7: Comparison of hindcast experiment upper ocean dFe concentration to observations in the equatorial Pacific. (a,d) average, (b,e) maximum, and (c,f) minimum modelled dFe values during the 1975-2021 time period (at monthly resolution); (a-c) zonal section at the equator, (d-f) meridional section at 140°W. Observations plotted on top (Coale et al., 1996; Fitzwater et al., 1996; Kaupp et al., 2011; Kondo et al., 2012; Mackey et al., 2002; Slemons et al. 2009, 2010; Wu et al., 2010). Some studies observe high dFe concentrations outside the model range, especially in the western part of the meridional section (a-c) and below ca. 100m, likely due to transport of Fe from the PNG region by the equatorial undercurrent (Slemons et al. 2009, 2010), whereas observations in the surface (i.e., upper ca. 100m) and the east (d-f) are generally within the modelled dFe range. Note that we chose a similar colour scheme as Slemons et al. 2009 to illustrate that our model resembles their "control" simulation.

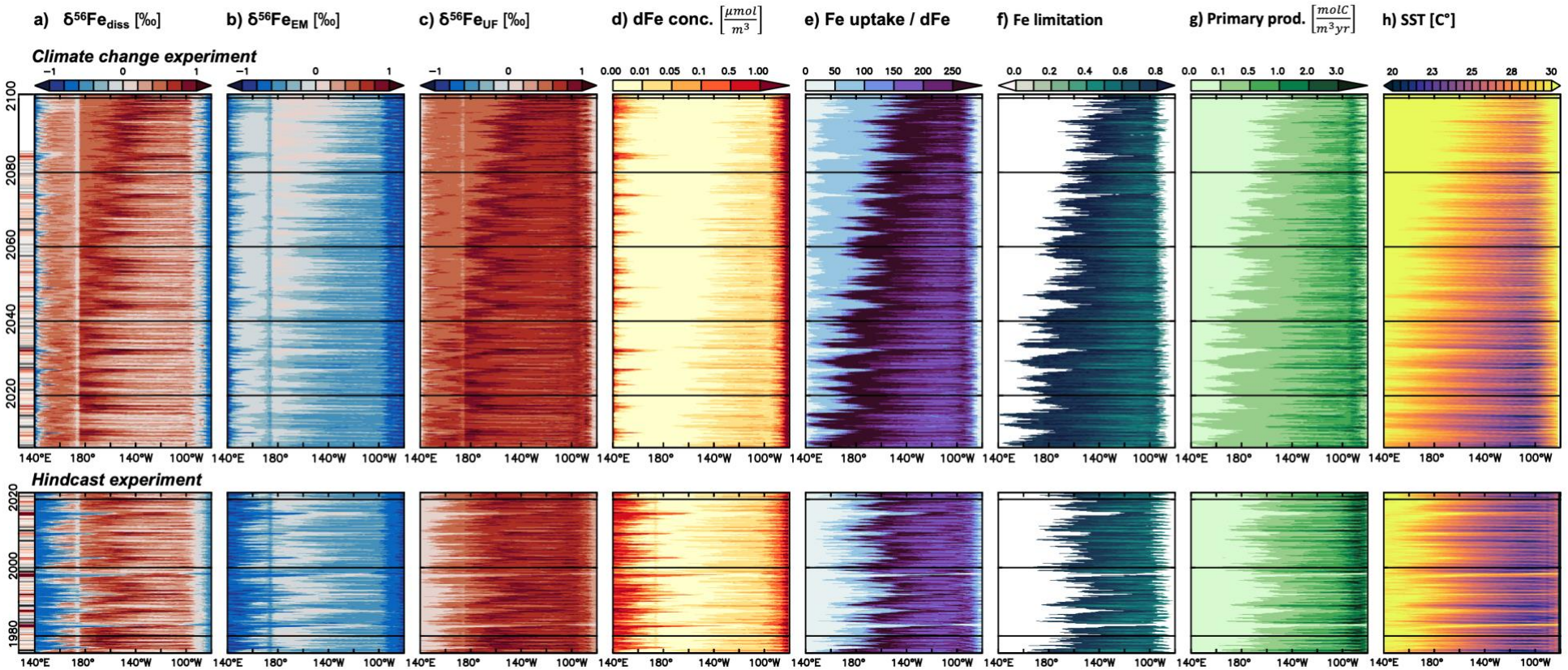

Figure S8: Mechanisms behind climate-change related surface ocean $\delta^{56}Fe_{diss}$ variability in the equatorial Pacific (at 0°). Upper section: Time series (2006-2100) of monthly-mean surface ocean (a) $\delta^{56}Fe_{diss}$, (b) $\delta^{56}Fe_{EM}$, (c) $\delta^{56}Fe_{UF}$, (d) dFe concentration, (e) ratio between Fe uptake and dFe concentration, (f) Fe limitation, (g) primary production, and (h) temperature of the climate change experiments. Lower section: Same parameters taken from the hindcast experiments. The Ocean Nino Index is included on the left side (red: El Niño, Grey: La Niña), whereby for the climate change experiment, the SST anomalies in the ENSO 3.4 region were calculated by subtracting 30 year running mean SST data from the monthly SST. Note that these plots were extracted from the equator (i.e., averaged over 0.5°S to 0.5°N instead of ±5°), as climate change induced $\delta^{56}Fe_{diss}$ changes are most pronounced here (Figure 2). Discrepancies between climate change and hindcast experiments, such as $\delta^{56}Fe_{diss}$ variability in the west, are due to differences in circulation patterns, which are most likely more realistic for the hindcast experiment, as it was forced by an atmospheric reanalysis product (see Figure S5)

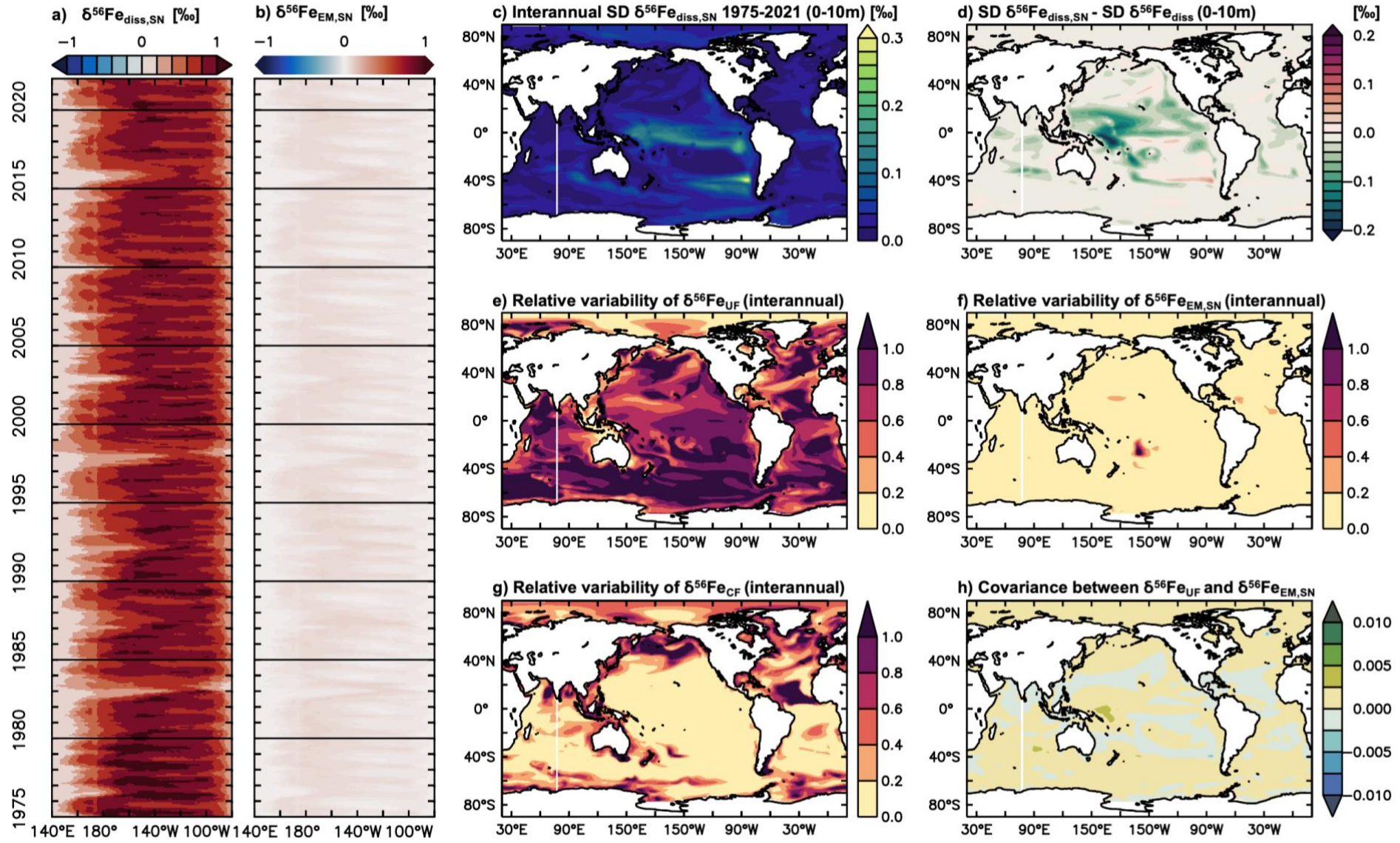

Figure S9: Impact of light sediment Fe on $\delta^{56}Fe_{diss}$ variability. Time series of surface ocean (a) $\delta^{56}Fe_{diss}$ and (b) $\delta^{56}Fe_{EM}$ in the tropical Pacific (5°S to 5°N average) for a hindcast experiment with neutral (0‰) sediment endmember (denoted a "SN"); (c) interannual SD $\delta^{56}Fe_{diss}$ of the same experiment, (d) difference between SD $\delta^{56}Fe_{diss,SN}$ and SD $\delta^{56}Fe_{diss}$ of the hindcast standard, ratios of interannual variability of (c) $\delta^{56}Fe_{UF}$, (d) $\delta^{56}Fe_{EM,SN}$, and (e) $\delta^{56}Fe_{CF}$ to the interannual $\delta^{56}Fe_{diss,SN}$ variability, and (f) covariance between $\delta^{56}Fe_{UF}$ and $\delta^{56}Fe_{EM,SN}$ (12-month running mean).

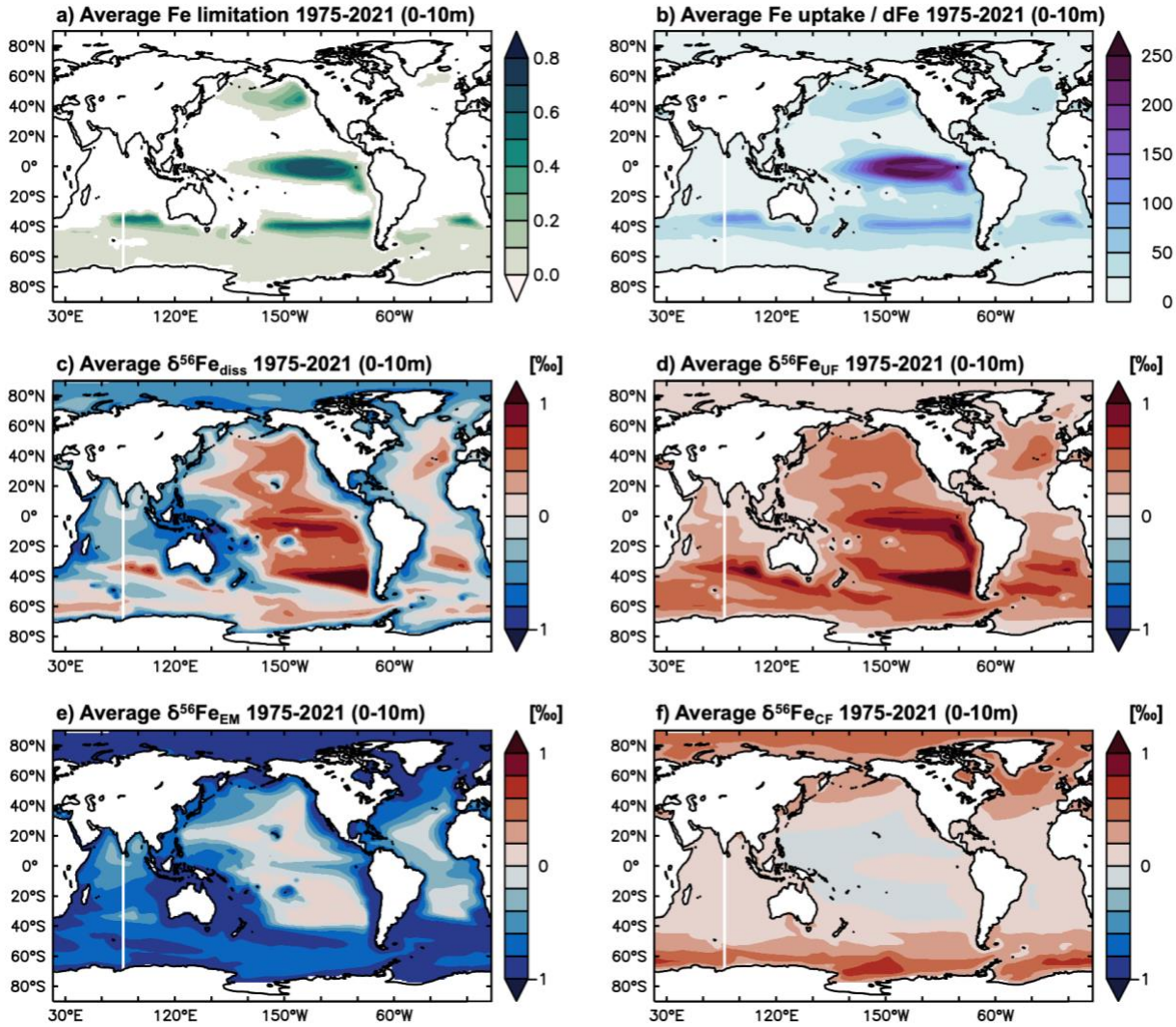

Figure S10. Connection between surface ocean Fe limitation and $\delta^{56}Fe_{diss}$ in the present climate (1975-2021). Surface ocean (0-10m) average values of (a) Fe limitation, (b) Fe uptake to dFe concentration ratio, (c) $\delta^{56}Fe_{diss}$, (d) $\delta^{56}Fe_{UF}$, (e) $\delta^{56}Fe_{EM}$ and (f) $\delta^{56}Fe_{CF}$ of the hindcast experiments. Note that Fe is usually limiting phytoplankton growth where the ratio between Fe uptake rates and dFe concentration is high, with some exceptions (e.g., in the North Atlantic). Meanwhile, a high Fe uptake to dFe concentration ratio generally leads to heavy $\delta^{56}Fe_{UF}$, although in some areas such as the south Pacific, $\delta^{56}Fe_{UF}$ is heavier than would be expected from this ratio.

References

Coale, K. H., Fitzwater, S. E., Gordon, R. M., Johnson, K. S., & Barber, R. T. (1996). Control of community growth and export production by upwelled iron in the equatorial Pacific Ocean. *Nature*, *379*, 621–624. https://doi.org/10.1038/379621a0

Fitzwater, S. E., Coale, K. H., Gordon, R. M., Johnson, K. S., & Ondrusek, M. E. (1996). Iron deficiency and phytoplankton growth in the equatorial pacific. *Deep-Sea Research Part II: Topical Studies in Oceanography*, *43*, 995–1015. https://doi.org/10.1016/0967-0645(96)00033-1

Kaupp, L. J., Measures, C. I., Selph, K. E., & Mackenzie, F. T. (2011). The distribution of dissolved Fe and Al in the upper waters of the Eastern Equatorial Pacific. *Deep-Sea Research Part II: Topical Studies in Oceanography*, *58*, 296–310. https://doi.org/10.1016/j.dsr2.2010.08.009

Kondo, Y., Takeda, S., & Furuya, K. (2012). Distinct trends in dissolved Fe speciation between shallow and deep waters in the Pacific Ocean. *Marine Chemistry*, *134–135*, 18–28. https://doi.org/10.1016/j.marchem.2012.03.002

Mackey, D. J., O'Sullivan, J. E. Os., & Watson, R. J. (2002). Iron in the western Pacific: A riverine or hydrothermal source for iron in the Equatorial Undercurrent? *Deep-Sea Research Part I: Oceanographic Research Papers*, *49*, 877–893. https://doi.org/10.1016/S0967-0637(01)00075-9

Slemons, L. O., Gorgues, T., Aumont, O., Menkes, C., & Murray, J. W. (2009). Biogeochemical impact of a model western iron source in the Pacific Equatorial Undercurrent. *Deep-Sea Research Part I: Oceanographic Research Papers*, *56*, 2115–2128. https://doi.org/10.1016/j.dsr.2009.08.005

Slemons, L. O., Murray, J. W., Resing, J., Paul, B., & Dutrieux, P. (2010). Western Pacific coastal sources of iron, manganese, and aluminum to the Equatorial Undercurrent. *Global Biogeochemical Cycles*, *24*, 1–16. https://doi.org/10.1029/2009GB003693

Wu, J., Wells, M. L., & Rember, R. (2010). Dissolved iron anomaly in the deep tropical-subtropical Pacific: Evidence for long-range transport of hydrothermal iron. *Geochimica et Cosmochimica Acta*, *75*, 460–468. https://doi.org/10.1016/j.gca.2010.10.024